npj | quantum information

Article

Published in partnership with The University of New South Wales

https://doi.org/10.1038/s41534-024-00944-4

# A mid-circuit erasure check on a dual-rail cavity qubit using the joint-photon number-splitting regime of circuit QED



Stijn J. de Graaf[1,2,5], Sophia H. Xue[1,2,5], Benjamin J. Chapman[1,2], James D. Teoh[2,3,4], Takahiro Tsunoda[1,2], Patrick Winkel[1,2], John W. O. Garmon[2,3], Kathleen M. Chang[1,2], Luigi Frunzio[1,2,4], Shruti Puri[1,2] & Robert J. Schoelkopf[1,2,3,4]

Quantum control of a linear oscillator using a static dispersive coupling to a nonlinear ancilla underpins a wide variety of experiments in circuit QED. Extending this control to more than one oscillator while minimizing the required connectivity to the ancilla would enable hardware-efficient multi-mode entanglement and measurements. We show that the spectrum of an ancilla statically coupled to a single mode can be made to depend on the joint photon number in two modes by applying a strong parametric beamsplitter coupling between them. This 'joint-photon number-splitting' regime extends single-oscillator techniques to two-oscillator control, which we use to realize a hardware-efficient erasure check for a dual-rail qubit encoded in two superconducting cavities. This scheme leverages the high-fidelity beamsplitter coupling already required for single- and two-qubit gates while permitting minimal crosstalk between circuit elements. Furthermore, the flexibility to choose the pulse shape allows us to limit the susceptibility to different error channels. We use this scheme to detect leakage errors with a missed erasure fraction of $(9.0 \pm 0.5) \times 10^{-4}$ while incurring an erasure rate of $2.92 \pm 0.01\%$ and a Pauli error rate of $0.31 \pm 0.01\%$, both of which are dominated by cavity errors.

Controlling the state of an oscillator is a powerful resource, enabling the implementation of hardware-efficient error-correcting codes for quantum computing[1–7], simulations of bosonic systems[8–12], and the generation of metrologically useful states for quantum-enhanced sensing[13–15]. In circuit quantum electrodynamics (cQED)[16,17], where these oscillators take the form of standing modes in microwave resonators, most of the techniques developed for single-oscillator control[18–25] rely on a static dispersive coupling between the oscillator and a nonlinear ancilla qubit[26].

Moving beyond the control of a single linear mode affords new capabilities, including the generation of multi-mode entanglement[27–29] and measurements of joint properties of multiple modes[30–33]. In the context of quantum error correction, it both enables gates between qubits encoded in individual modes[34,35], as well as implementations of natively multi-mode error correcting codes, such as the pair-cat[36], Chuang–Leung–Yamamoto (CLY)[37], or dual-rail codes[38]. This may be done by complementing the dispersive control with tunable beamsplitter interactions[39], which swap states between oscillators, allowing the nonlinear ancilla to interact with each oscillator in turn.

Recent progress in generating stronger tunable beamsplitter interactions between high-$Q$ cavities without compromising their long coherence times or introducing unwanted nonlinearity[40,41] provides access to a regime where the inter-oscillator coupling strength exceeds the typical coupling strength to the nonlinear ancilla. This presents the opportunity to treat the coupled oscillators collectively. Thus a single ancilla, statically coupled to only one of the modes, can be used to measure either joint or individual properties of the combined system. Such operations include the recently proposed joint-parity measurement or erasure check of a dual-rail cavity qubit[42,43].

In this article, we observe a new regime that emerges in the presence of an increasingly strong beamsplitter drive between two bosonic modes, which is an analog of dispersive number splitting[26], but for the total excitation number, $N$, shared between two modes. In this regime, the eigenmodes of the combined multi-mode system become the symmetric and anti-symmetric combinations of the bare resonator modes, thereby matching the dispersive coupling strength between each eigenmode and the nonlinear ancilla. We find a range of operating points that are now accessible

[1]Department of Applied Physics, Yale University, New Haven, CT, 06511, USA. [2]Yale Quantum Institute, Yale University, New Haven, CT, 06511, USA. [3]Department of Physics, Yale University, New Haven, CT, 06511, USA. [4]Quantum Circuits Inc., 25 Science Park, New Haven, CT, 06511, USA. [5]These authors contributed equally: Stijn J. de Graaf, Sophia H. Xue. e-mail: robert.schoelkopf@yale.edu

where we can measure the total photon number in the coupled oscillators, without measuring the photon number in either cavity.

An important example of an operation enabled in this regime is a mid-circuit erasure check[33,44], an essential ingredient for a dual-rail qubit[38] spanned by the single excitation manifold $|0,1\rangle$ and $|1,0\rangle$ of two superconducting cavity modes. Erasure qubits[33,43–51] rely on detecting dominant leakage errors and resetting these states back into the codespace. Since the time and location of these (erasure) errors are known, erasure qubits yield high thresholds when embedded in a higher-level error-correcting code[48,52,53]. The dual-rail cavity qubit is a prototypical example of this as its errors are dominated by detectable leakage to $|0,0\rangle$, with Pauli errors within the codespace much less likely[43].

We implement a minimally invasive erasure check by only exciting the less-coherent ancilla transmon when the dual-rail qubit has already leaked from the codespace. This limits the probability of declaring an erasure due to errors in the measurement itself to $2.92 \pm 0.01\%$ per check, of which only $0.51 \pm 0.02\%$ are false positives due to transmon errors. With a missed-erasure probability of only $(9.0 \pm 0.5) \times 10^{-4}$, dual-rail logical states are also well-preserved, with a Pauli error rate of $0.31 \pm 0.01\%$, of which only $0.12 \pm 0.01\%$ is induced by transmon decoherence. As in the previous demonstration of mid-circuit erasure detection for a dual-rail cavity qubit by Koottandavida et al.[33], this scheme engineers an ancilla spectrum that distinguishes between computational states and the joint vacuum state, $|0,0\rangle$. However, it does not use a separate "$\chi$-matching" drive[23] but makes use of the tunable beamsplitter in a unit cell already containing all the hardware required for single- and two-qubit gates. Importantly, in this architecture, the only oscillator–oscillator coupling is a high-fidelity beamsplitter between adjacent modes, providing a way to minimize crosstalk as well as ZZ errors during two-qubit gates. Realizing such a high-performance and minimally invasive mid-circuit erasure check is a crucial capability for improving error correction[48] via erasure conversion.

In the following sections, we begin by describing the emergence of parametrically activated joint-photon number-splitting, before showing its application in a dual-rail erasure check. An extension of this technique to a two-qubit gate is described in Appendix B.

## Results

### Spectroscopic observation of joint-photon number-splitting

Combining two common elements of oscillator control, a tunable beamsplitter interaction between two oscillators and a fixed dispersive interaction between a single oscillator and an ancillary qubit, enables measurements and control conditioned on the total photon number of the system, via an extension of the strong dispersive regime of circuit QED[26]. The Hamiltonian of this system in the interaction picture is

$$\frac{\hat{\mathcal{H}}}{\hbar} = \frac{g_{\mathrm{bs}}(t)}{2}\left(e^{i\varphi}\hat{a}\hat{b}^{\dagger} + e^{-i\varphi}\hat{a}^{\dagger}\hat{b}\right) - \Delta\hat{b}^{\dagger}\hat{b} + \chi\hat{b}^{\dagger}\hat{b}|e\rangle\langle e|, \tag{1}$$

where the oscillator Alice and Bob modes are represented by lowering operators $\hat{a}$ and $\hat{b}$, and $|e\rangle$ is the excited state of the ancillary qubit (see Fig. 1a). The ancilla is coupled to only one of the modes with a dispersive interaction strength $\chi$ that is fixed, whereas the amplitude $g_{\mathrm{bs}}$, phase $\varphi$ and frequency detuning $\Delta$ of the beamsplitter drive are all controllable in time. In order to perform joint-photon-number-selective operations, we will specifically consider the case where $\Delta = \chi/2$. Since the Bob oscillator frequency shifts by $\chi$ when the ancilla is in $|e\rangle$, this special operating point ensures the beamsplitter drive is equally detuned from resonance when the ancilla is in $|g\rangle$ or in $|e\rangle$. With this choice of detuning (and with the drive

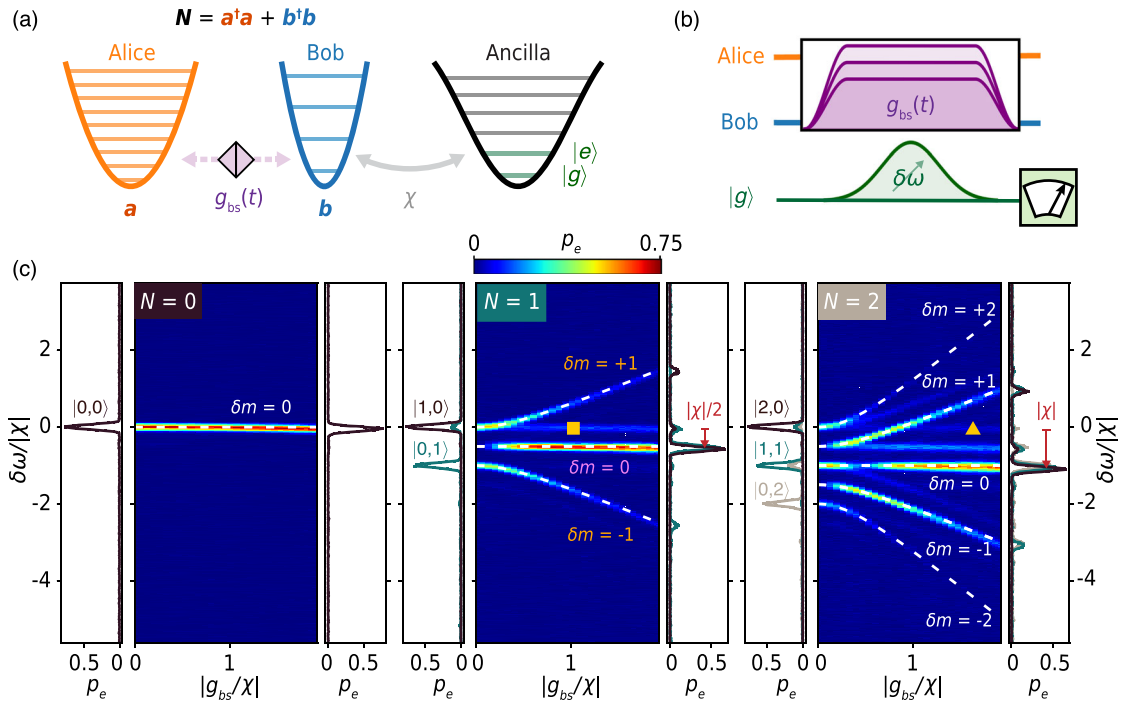


**Fig. 1 | Ancilla spectroscopy in the presence of a beamsplitter drive. a** System schematic showing two oscillators coupled by a tunable beamsplitter interaction and an ancilla qubit statically coupled to one oscillator via a fixed dispersive interaction. **b** Pulse sequence used for spectroscopy experiment. **c** Transmon spectra in the presence of increasing beamsplitter drive amplitude for input oscillator states with fixed total photon number $N$. Colorplots show initial states $|0,0\rangle$ $(N=0)$, $\frac{|0,1\rangle+|1,0\rangle}{\sqrt{2}}$ $(N=1)$, and $\frac{|0,2\rangle+\sqrt{2}|1,1\rangle+|2,0\rangle}{2}$ $(N=2)$. Predicted transitions (dashed white lines) are labeled by $\delta m$, the change in the photon number difference between the symmetric and anti-symmetric eigenmodes of the coupled oscillators (see Eq. (6)). Faint lines corresponding to transitions in the $(N-1)$-photon manifold may be seen in the $N=1$ and $N=2$ spectra due to photon loss during the spectroscopy pulse. Left (right) panels show spectra for all initial two-oscillator Fock states in each $N$-photon manifold at the lowest (highest) value of $|g_{\mathrm{bs}}/\chi|$ shown in the colorplots. Red arrows in the right panels of the $N=1$ and $N=2$ spectra show the central transition frequency moving by $\delta\omega = N\chi/2$ in the joint-photon number-splitting regime. The yellow square (triangle) in the $N=1$ $(N=2)$ panel indicates operating point for the erasure check (CPHASE gate described in Appendix B).

phase set to $\varphi = 0$), the Hamiltonian in Eq. (1) simplifies to

$$\frac{\hat{\mathcal{H}}}{\hbar} = \frac{g_{\rm bs}(t)}{2}\left(\hat{a}\hat{b}^{\dagger} + \hat{a}^{\dagger}\hat{b}\right) - \chi\hat{b}^{\dagger}\hat{b}\frac{\hat{\sigma}_z}{2}, \tag{2}$$

where $\hat{\sigma}_z = |g\rangle\langle g| - |e\rangle\langle e|$.

This Hamiltonian is realized with a pair of superconducting microwave stub cavities as the oscillators[54] and a fixed-frequency transmon as the ancilla. The use of a SNAIL coupler[40,55–57] situated between the cavities allows us to engineer a microwave-activated beamsplitter interaction with amplitude up to $g_{\rm bs}/2\pi = 2.05$ MHz, higher than that of the dispersive coupling $\chi/2\pi = -1.07$ MHz, while preserving the coherence and linearity of the cavity modes.

The dispersive term (activated by intentionally exciting the ancilla out of its ground state) and the beamsplitter term are often used alternately: either narrow-bandwidth pulses on the ancilla enact photon-number-selective operations on a single mode or a beamsplitter routes states between modes[28]. However, when both terms are activated simultaneously and $g_{\rm bs} \sim |\chi|$, the number-split spectrum of the ancilla is modified to depend on the joint photon number in both oscillators.

The emergence of joint-photon number-splitting is revealed by probing the transmon spectrum in the presence of a variable-amplitude beamsplitter drive, as illustrated in Fig. 1b. Because the Hamiltonian conserves the total oscillator photon number $N$ and the average cavity $T_1$ is much longer than the pulse duration $T_{\rm p}$, the dynamics may be considered separately for different values of $N$. Figure 1c shows the resulting spectra for different initial states with $N = 0$, 1 and 2. In the absence of a coupling between the cavities ($g_{\rm bs} = 0$) the transmon spectrum displays the familiar photon number-splitting regime, with transitions separated in frequency by $\chi$ per photon in the Bob mode but independent of the photon number in the uncoupled Alice mode. This can be seen from the linecuts at $g_{\rm bs} = 0$ (in the left panels of Fig. 1c) when initializing the cavities in different two-oscillator Fock states. However, in the presence of a strong beamsplitter drive, $(g_{\rm bs} \sim |\chi|)$ we enter the joint-photon number-splitting regime. Here, the transmon spectrum exhibits $2N+1$ prominent transition lines, with a dominant central transition emerging at large values of $g_{\rm bs}$, when the spectroscopy tone is detuned from the bare transmon resonance by an amount $\delta\omega = N\chi/2$.

We can compare these features to analytical predictions obtained by considering the normal modes of the coupled oscillators. When the amplitude of the spectroscopy pulse is small relative to $\max(g_{\rm bs}, |\chi|)$, its effect may be treated as a perturbation to the Hamiltonian in Eq. (2), which is block-diagonal with respect to the ancilla subspace:

$$\hat{\mathcal{H}} = \hat{\mathcal{H}}_{\rm g}|g\rangle\langle g| + \hat{\mathcal{H}}_{\rm e}|e\rangle\langle e|. \tag{3}$$

Diagonalizing $\hat{\mathcal{H}}_g$ and $\hat{\mathcal{H}}_e$ allows us to find new eigenmodes conditioned on the state of the ancilla:

$$\begin{aligned} \hat{\Sigma}_g &= \hat{a}\cos(\theta) + \hat{b}\sin(\theta) \quad \hat{\Sigma}_e = \hat{b}\cos(\theta) + \hat{a}\sin(\theta) \\ \hat{\Delta}_g &= \hat{b}\cos(\theta) - \hat{a}\sin(\theta) \quad \hat{\Delta}_e = \hat{a}\cos(\theta) - \hat{b}\sin(\theta) \end{aligned} \tag{4}$$

where the mixing angle $\theta = \arctan(2g_{\rm bs}/\chi)/2$. In the $g_{\rm bs} \gg \chi$ limit, the $\hat{\Sigma}_i$ and $\hat{\Delta}_i$ modes tend to symmetric ($\hat{\Sigma} = (\hat{a} + \hat{b})/\sqrt{2}$) and antisymmetric ($\hat{\Delta} = (\hat{a} - \hat{b})/\sqrt{2}$) combinations of the bare oscillator modes. In terms of these operators, the ancilla-state-dependent Hamiltonians may be written as

$$\begin{aligned} \frac{\hat{\mathcal{H}}_g}{\hbar} &= -\frac{\chi}{2}\left(\frac{\hat{\Sigma}_g^{\dagger}\hat{\Sigma}_g + \hat{\Delta}_g^{\dagger}\hat{\Delta}_g}{2}\right) + \Omega\left(\frac{\hat{\Sigma}_g^{\dagger}\hat{\Sigma}_g - \hat{\Delta}_g^{\dagger}\hat{\Delta}_g}{2}\right), \\ \frac{\hat{\mathcal{H}}_e}{\hbar} &= +\frac{\chi}{2}\left(\frac{\hat{\Sigma}_e^{\dagger}\hat{\Sigma}_e + \hat{\Delta}_e^{\dagger}\hat{\Delta}_e}{2}\right) + \Omega\left(\frac{\hat{\Sigma}_e^{\dagger}\hat{\Sigma}_e - \hat{\Delta}_e^{\dagger}\hat{\Delta}_e}{2}\right), \end{aligned} \tag{5}$$

where $\Omega = \sqrt{g_{\rm bs}^2 + (\chi/2)^2}$. (We have ignored the dependence of $\chi$ on the frequency detuning between the ancilla mode and the cavity modes. In principle, if $g_{\rm bs}$ became large enough to be comparable to this detuning, then the symmetric and antisymmetric modes would have meaningfully different detunings to the transmon and so would not have matched dispersive shifts. In our system, where the frequency detuning is ~2 GHz, and $g_{\rm bs}/2\pi$ is at most 2 MHz, this is not a concern.)

For a particular ancilla state, the oscillator eigenstates are then defined by two quantities: half the total photon number in the two modes, $N/2$, and half the difference in the photon number occupation of the symmetric and antisymmetric modes, described by the operator,

$$\hat{m}_i \equiv \frac{\hat{\Sigma}_i^{\dagger}\hat{\Sigma}_i - \hat{\Delta}_i^{\dagger}\hat{\Delta}_i}{2}, \tag{6}$$

for $i \in \{g, e\}$, which can take values $m_i = -N/2, \ldots, N/2$. For a fixed total photon number $N$, the ancilla energy levels display an $(N+1)$-fold splitting by an amount $\Omega$, as illustrated in Fig. 2 for the case $N = 1$.

The energy difference between each possible pair of $\hat{\mathcal{H}}_g$ and $\hat{\mathcal{H}}_e$ eigenstates allows us to accurately predict the $2N+1$ unique transitions observed in the spectra:

$$\delta\omega_{\delta m} = \frac{N}{2}\chi + \delta m\,\Omega, \tag{7}$$

labeled by $\delta m \equiv m_e - m_g = -N, \ldots, N$. These frequencies are shown as white dashed lines in Fig. 1c and show good agreement with the observed spectra. Faint features corresponding to transitions in the $N-1$ photon manifold can also be seen due to photon loss during the spectroscopy pulse. The symmetric beamsplitter detuning condition $\Delta = \chi/2$ provides a unique operating point where each transition frequency has a degeneracy $(N+1)-|\delta m|$. (We note that the spectrum for $N = 1$ is reminiscent of the Mollow triplet[58,59] seen when probing the frequency of strongly-driven two-level-system. Here, we are instead probing the frequency of a two-level-system that is dispersively coupled to the strongly driven mode. In Appendix E, we show how shifting

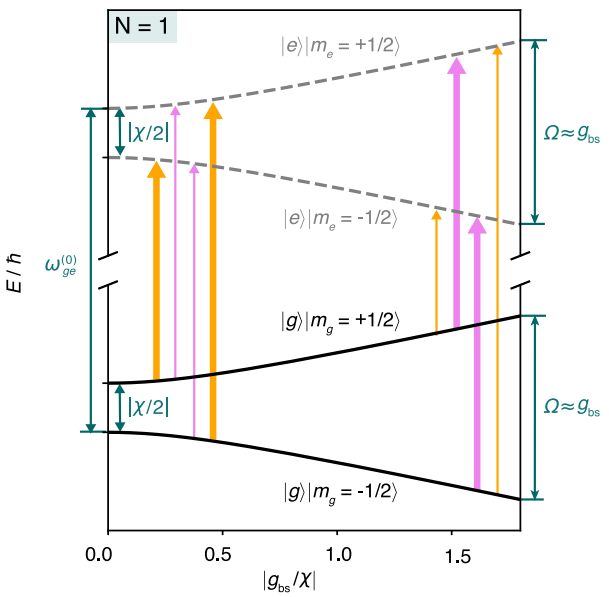


**Fig. 2 | Energy level diagram in the presence of beamsplitter drive.** Energy level diagram when $N = 1$ photons are shared between the two oscillators. The transmon state is labeled by $|g\rangle$ or $|e\rangle$ and the two-oscillator state is labeled by its value of $m$, which describes the relative photon number occupation of the symmetric and antisymmetric modes of the two oscillators (see Eq. (6)). The $|g\rangle$ and $|e\rangle$ levels, separated by $\omega_{ge}^{(0)}$ in the absence of any coupling to the oscillators, are now split by $\Omega = \sqrt{g_{\rm bs}^2 + (\chi/2)^2}$. Vertical arrows indicate possible transitions for which $\delta m \equiv m_e - m_g = 0$ (pink) and $\delta m = \pm 1$ (orange). Arrow thicknesses illustrate the strength of transition matrix elements at low and high beamsplitter amplitudes.

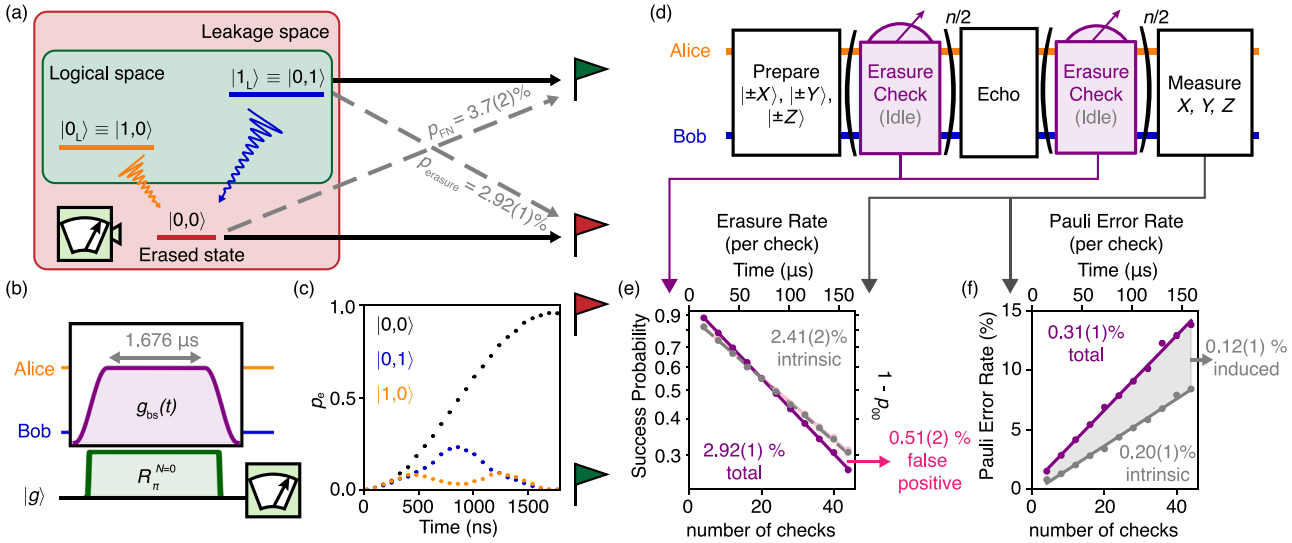


**Fig. 3 | Characterizing a dual-rail mid-circuit erasure check. a** Logical code space of a dual-rail encoded qubit indicating decay to the leakage state $|0, 0\rangle$, which we seek to detect and convert to erasure errors. Black arrows show the ideal mapping processes while gray arrows indicate misassignment processes that lead to false negative (FN) errors and erasure errors, respectively. We measure a false negative probability of $p_{FN} = 3.7(2)\%$ and a total erasure error rate of $p_{erasure} = 2.92(1)\%$ per erasure check. Green (red) flag indicates an erasure check reporting "no erasure" ("erasure detected"). **b** Pulse sequence used to implement the erasure check, consisting of simultaneous flat-top pulses on both the transmon and the beamsplitter drive, followed by transmon readout. **c** Measured transmon trajectories during the erasure check for logical and leakage states. **d** Pulse sequence used to measure state fidelity after $n$ repeated erasure checks (or $n$ periods of idling for the duration of an erasure check) on the encoded dual-rail qubit. A single echo pulse (a cavity SWAP operation) is performed halfway through the sequence in order to suppress the effect of no-jump backaction resulting from different cavity decay rates. **e** Success probability for passing $n$ consecutive checks (purple), and probability of remaining in logical subspace ($1-p_{00}$) after $n$ checks, unconditioned on erasure check results, with (gray) and without (pink) the beamsplitter pump applied. **f** Total Pauli error rate when performing erasure checks (purple) or idling (gray). Lines show linear fits.

away from this detuning breaks the degeneracies between these transitions, yielding $(N+1)^2$ unique frequencies.)

Furthermore, the strength of each transition is proportional to the overlap between the initial ($\hat{\mathcal{H}}_g$) and final ($\hat{\mathcal{H}}_e$) oscillator eigenstates. As $g_{bs}$ is increased relative to $|\chi|$, the ancilla-state-dependent eigenmodes approach one another, with $\hat{\Sigma}_g \to \hat{\Sigma}_e$, $\hat{\Delta}_g \to -\hat{\Delta}_e$ and, consequently, $\hat{m}_g \to \hat{m}_e$. The overlap between initial and final states satisfying $m_g = m_e$ therefore increases towards 1. As a result, off-central transitions with $\delta m \neq 0$ become suppressed in favor of transitions with $\delta m = 0$, as can be seen from their changing brightness in Fig. 1c. The magnitude of the transition matrix elements is also indicated by the thickness of the arrows in Fig. 2. In Appendix D, we show that the measured transition matrix elements agree very well with analytical predictions. While compact analytical expressions for these matrix elements can be derived in this normal modes picture, they are more readily obtained by considering the Schwinger representation of two coupled oscillators as a single spin with $s = N/2$[60]. This alternative interpretation, in which the beamsplitter drive applies a Zeeman shift to the spin, is discussed in detail in Appendix A.

The predictions of both the transition frequencies and their matrix elements explain the emergence of a joint-photon number-splitting regime when $g_{bs} \gtrsim |\chi|$, where the qubit spectrum depends on the total photon number in both oscillators. This is most clear in the linecuts of the spectra at the largest values of $g_{bs}/|\chi|$ in Fig. 1, where independent of which state is initialized in the oscillators, we see a single dominant transition frequency at $\delta\omega = N\chi/2$ for each value of $N$. In this regime, the system consists of a symmetric and antisymmetric mode, each with a dispersive shift of $\chi/2$ to the ancilla

$$\frac{\hat{\mathcal{H}}}{\hbar} \xrightarrow{g_{bs} \gg |\chi|} \left(+\frac{g_{bs}}{2} - \frac{\chi}{2}\frac{\hat{\sigma}_z}{2}\right)\hat{\Sigma}^\dagger\hat{\Sigma} + \left(-\frac{g_{bs}}{2} - \frac{\chi}{2}\frac{\hat{\sigma}_z}{2}\right)\hat{\Delta}^\dagger\hat{\Delta}. \quad (8)$$

Photons in Alice and Bob are thus indistinguishable from the perspective of the qubit when the beamsplitter interaction is stronger than the dispersive shift. The extent to which the qubit can still distinguish the two oscillators can be seen in the much smaller satellite peaks at $\delta m = \pm\Omega$, which would be further suppressed at higher beamsplitter amplitudes.

In the following section, we show how understanding these joint-photon number-split spectra provides a way to extend established single-oscillator control techniques to operations on multiple oscillators.

## Mid-circuit erasure check of a dual-rail qubit

We use the $|g_{bs}| \gtrsim |\chi|$ regime to construct a mid-circuit erasure check for a dual-rail qubit encoded in two superconducting cavities. The basis states for this encoding are $|0_L\rangle \equiv |1, 0\rangle$ and $|1_L\rangle \equiv |0, 1\rangle$ and their dominant error channel is photon loss to the common $|0, 0\rangle$ leakage state, which we hope to detect (see Fig. 3a). Detecting these leakage errors (in order to convert them to erasures) while preserving logical information in states that have not suffered such an error is an essential task in this architecture.

A key requirement of the erasure check is that it does not introduce additional errors. Firstly, since the check may be performed multiple times per round of syndrome measurements, erasure errors during the check must be minimized for the code to operate below the error-correction threshold of the higher-level code, such as the surface code[61–63]. Secondly, Pauli errors must remain much less likely than erasure errors to preserve the bias that enables a high threshold[48]. Both of these criteria require a way of limiting errors induced by the less-coherent ancilla transmon.

A powerful and established technique for measuring bosonic modes while preventing the ancilla from polluting the logical state is to use a three-level ancilla and to apply a microwave drive to ensure that the dispersive shift is unchanged when the ancilla is in $|e\rangle$ or in $|f\rangle$ (often known as $\chi$-matching)[23]. This erasure check, however, bypasses the need for $\chi$-matching drives since it only needs to catch events when the logical information has already been lost.

The modification of the transmon spectrum in the presence of a beamsplitter drive allows us to perform an erasure check with low susceptibility to transmon errors. In the number-splitting regime for a single oscillator, a narrow-bandwidth pulse on the ancilla enables an $\pi$-pulse conditioned on zero photons in the oscillator. Likewise, the joint-photon

number-splitting regime allows us to excite the transmon if and only if there are zero total photons in two oscillators (i.e. when the dual-rail qubit has leaked to $|0,0\rangle$).

For transmon pulses selective on $N=0$, we do not require $g_{bs} \gg \chi$ but only that the $N=0$ transition is sufficiently detuned from all other transitions, we would like to avoid. In the context of the dual-rail encoding, these are the transitions in the $N=1$ manifold (corresponding to the logical subspace). For beamsplitter drive amplitudes $g_{bs}/|\chi| \geq \sqrt{3}/2$, the nearest transition we wish to avoid is the central ($N=1$, $\delta m=0$) transition which is detuned from our desired $N=0$ resonance by an amount $|\chi|/2$ (see Fig. 1c). This establishes a wide range of values for $g_{bs}/|\chi|$ that can enact an erasure check and allows for a more flexible implementation than the erasure check proposed in[42,43], based on measuring the joint photon number parity, where $|g_{bs}/\chi|$ is fixed. This allows us to both avoid specific values of $g_{bs}$ at which multiphoton transitions degrade the cavity coherences[64] and increase $g_{bs}$ to suppress transmon-induced Pauli errors by making the two oscillators more indistinguishable from the perspective of the qubit (see Appendix J).

More crucially, unlike with the joint-parity approach, we have the flexibility to use a variety of pulse shapes on the transmon drive to perform the erasure check while trading off susceptibility to different error sources (see Appendix K for a detailed comparison of the two approaches). For example, a long, highly frequency-selective Gaussian pulse will limit transmon excitation when in the $N=1$ manifold, reducing false positive and Pauli errors due to transmon decoherence, at the expense of more idling errors during the check. To minimize the combined rate of transmon errors and idling errors, we use a shorter square pulse with a duration $T_p = 1.820\,\mu s$ while applying a beamsplitter drive with amplitude $|g_{bs}/\chi| = 1.04$ (as indicated by the square symbol in Fig. 1c). These values of $g_{bs}$ and $T_p$ are calibrated to ensure that when starting in the dual-rail logical subspace, both the transmon and oscillators return to their initial states at the end of the sequence, while avoiding the slight degradation in cavity coherence at higher $g_{bs}$[40] (see Fig. 3b, c; for detailed calibration procedures, see Appendix F). While this scheme places no special requirement on the adiabaticity of the beamsplitter drive ramp, we use a 120 ns cosine-shaped ramp to stay well within the bandwidth limit imposed by the on-chip Purcell filter through which the beamsplitter drive is applied. We align the center of this ramp in time with the center of the 24 ns cosine ramp on the transmon pulse, which we find from simulation ensures optimal performance.

The trajectories of the transmon state for different input oscillator states in Fig. 3c showcase the operation of the erasure check: while the transmon ends in $|e\rangle$ when the oscillators are in $|0,0\rangle$ (thus flagging an erasure), it returns to $|g\rangle$ for input states $|0,1\rangle$ and $|1,0\rangle$. The relatively small area under the $|0,1\rangle$ and $|1,0\rangle$ curves indicates that the transmon is less likely to be excited in these cases and so transmon decay and dephasing errors are less likely to induce false positives or logical Pauli errors. Meanwhile the relatively small difference between the $|0,1\rangle$ and $|1,0\rangle$ curves indicates the limited extent to which transmon dephasing errors allow the environment to distinguish between different logical states, thereby inducing Pauli errors when they occur[65].

We test the fraction of leakage errors caught by the check by preparing $|0,0\rangle$ and performing a single mid-circuit erasure check followed by destructive photon-number-selective measurements of each cavity[44]. When post-selecting on the final state remaining in $|0,0\rangle$, we find a false negative probability (i.e. the probability of not flagging an erasure *conditioned on* a leakage state input, as illustrated in Fig. 3a) $p_{FN} = 3.7 \pm 0.2\%$, consistent with results of master equation simulations using the physical transmon error rates in our system. While the false negative probability *is* sensitive to transmon decoherence, in the operation of an error-correcting code the actual probability of missing an erasure ($p_{miss} = p_{erasure} \times p_{FN} \sim 10^{-3}$) is also multiplied by the very small probability that an erasure has been suffered since the previous check. We find that this false negative probability is still admissible for high fault-tolerant thresholds in the surface code. In fact, when performing erasure checks after every two-qubit gates, the surface code threshold (per step consisting of a gate plus an erasure check) with such a level of false negatives is $p_{th} = 3.71 \pm 0.02\%$, as compared to $p_{th} = 3.79 \pm 0.02\%$ if the false negative probability were 0. This indicates that the threshold is minimally affected by the observed false negative probability and remains well in excess of the 1% Pauli noise threshold. In both cases, we have assumed that 90% of errors are erasures. For more details on these simulations, refer to Appendix G. As such, an increase in $p_{FN}$, which has a very small impact on $p_{th}$, is less costly than an equivalent increase in $p_{FP}$, which adds to the overall physical error rate that should be kept small with respect to $p_{th}$. This informs the design of the erasure check where the transmon is excited if and only if $N=0$.

A single experiment is used to evaluate the performance of the mid-circuit erasure check when acting on the code space, in terms of both the erasure error rate and the Pauli error rate induced by the check. This tomography sequence, shown in Fig. 3d, consists of preparing the six dual-rail cardinal states $|\pm X\rangle, |\pm Y\rangle$, and $|\pm Z\rangle$, repeating the erasure check $n$ times and then measuring the logical operators $\hat{X}_L, \hat{Y}_L$ and $\hat{Z}_L$ using photon-number-selective readout of each cavity (see Appendix H). To separate the contribution from idling errors, we perform the same sequence but replace each erasure check with a delay of the same duration. Beamsplitter pulses are used to enact single-qubit gates on the dual-rail qubit, allowing us to prepare states on the equator of the Bloch sphere and perform logical measurements. An echo pulse is added to remove the effect of no-jump back-action at long times. When the decay rate in each cavity is different (as is especially the case here, with $T_{1,a} = 347\,\mu s$ and $T_{1,b} = 109\,\mu s$), post-selecting on no photon loss leads to a deterministic polarization towards one pole of the Bloch sphere and results in an approximately-Gaussian envelope on both the idling and erasure check data on a timescale set by the difference in the $T_1$ times[43]. Introducing the echo therefore allows us to better resolve errors induced by the check itself.

The erasure rate is extracted by looking at the success probability (i.e. the likelihood of passing $n$ successive checks) as a function of $n$, averaged over all input states (see Fig. 3e). The slope of the exponential decay shows a total erasure rate per check $p_{erasure} = 2.92 \pm 0.01\%$. To determine what fraction of these flagged events are 'intrinsic' erasures due to photon loss to $|0,0\rangle$, as opposed to false positive events predominantly due to transmon errors, we may instead ignore the results of the mid-circuit checks and only ask how often the end-of-line measurement yields $|0,0\rangle$. This gives a photon loss rate of $2.41 \pm 0.02\%$ per check, consistent with the value obtained when idling for the same duration, $2.43 \pm 0.02\%$, indicating that the erasure check does not induce additional photon loss in the cavities. This value is the 'intrinsic' erasure rate, from which we infer that the remaining $0.51 \pm 0.02\%$ of erasures are false positive errors. That the majority of detected erasures are due to photon loss in the high-$Q$ cavities, rather than transmon errors, shows the ability of the scheme to tolerate decoherence in the transmon ancilla. Furthermore, the flexibility to choose different transmon pulse shapes allows us to trade-off between 'intrinsic erasures' due to cavity relaxation (suppressed with a shorter pulse) and false positives due to transmon decoherence (suppressed with a longer, more selective pulse), which we can therefore tailor to minimize the total erasure rate. In principle, a shorter-duration joint-parity measurement[42] would be optimal when the oscillator decoherence is comparable to that of the transmon, however it is expected that the oscillator should always be significantly longer-lived (see Appendix K). This flexibility, not present in the joint-parity-based approach, also allows us to trade a reduction in the false positive probability ($p_{FP} = 0.51\%$) for an increase in the less-costly false negative probability ($p_{FN} = 3.7\%$).

To verify that this mid-circuit erasure check preserves the logical qubit state, we probe the fidelity of all 6 dual-rail cardinal states conditioned on passing $n$ successive erasure checks. Fitting the slope of the post-selected Pauli error probabilities (obtained from the average state fidelity; see Appendix I) as a function of measurement rounds $n$ allows us to precisely resolve the error rate for a single round (Fig. 3f). We find that the logical information is well-preserved during the course of the measurement, with an overall Pauli error per check $p_{Pauli} = 0.31 \pm 0.01\%$, compared to $0.20 \pm 0.01\%$ when idling. This indicates that background cavity errors dominate, with transmon-induced Pauli errors contributing at most the

remaining 0.12 ± 0.01%, highlighting the robustness of the scheme against transmon decoherence. We note that while the echo pulse used to mitigate against no-jump backaction will also reduce the effect of low-frequency dephasing noise on the intrinsic error rate, errors induced by transmon decoherence should not be affected.

Taken together, these results demonstrate the efficacy of a flexible hardware-efficient mid-circuit erasure check, making use of only the beamsplitter interaction (used for gates) and dispersive transmon coupling to a single mode (used for state preparation). This check preserves a large ratio of the erasure error rate to the Pauli error rate, with both quantities remaining dominated by 'intrinsic' errors associated with the hardware, and has a false negative probability that only negligibly reduces $p_{\mathrm{th}}$ from its value with perfect detection. With improvement of the mode coherences closer to state-of-the-art values[66–68], we expect this scheme to yield significantly below-threshold performance. Indeed, with the same $\chi$, $g_{\mathrm{bs}}$, and readout duration $\tau_{\mathrm{RO}}$ but with a transmon $T_1$ and $T_\phi$ of 200 μs and an average cavity $T_1$ of 1000 μs, we predict from master equation simulations a total erasure rate $p_{\mathrm{erasure}} = 0.49\%$ and a transmon-induced Pauli error rate of 0.035%, at which point shot-noise dephasing from photons in the readout resonator starts playing a larger role (see Appendix L). Increasing $\chi$ and reducing $\tau_{\mathrm{RO}}$ to reduce the check duration provides another way to improve performance. Separately, we could leverage the flexibility of this scheme to increase $g_{\mathrm{bs}}$, since this helps reduce Pauli errors from transmon dephasing by making the dual-rail logical states more indistinguishable during the check[65] (see Appendix J).

## Discussion

These results show that a strong beamsplitter drive, when paired with dispersive coupling to a single mode, offers a versatile means of measuring and controlling multiple oscillators. The tunable beamsplitter allows for switching between single-cavity operations (accessible when $g_{\mathrm{bs}} = 0$) and their equivalent multi-cavity operations on the total photon number (accessible when $g_{\mathrm{bs}} \gtrsim \chi$). As an important example of this, we have demonstrated how photon-number selective measurements can be extended to joint-photon-number selective measurements to enable a mid-circuit erasure check for dual-rail qubits. Further examples of this principle include the extension of the "selective number arbitrary phase" (SNAP) gate to a joint-SNAP-like gate selective on the photon number in two cavities, enabling a tunable CPHASE($\theta$) gate for two dual-rail qubits (see Appendix B).

The mid-circuit erasure check for dual-rail qubits enabled by joint-photon-number selective measurements represents a new, hardware-efficient way of performing the essential ingredient for an error-correcting surface code with dual-rail cavity qubits. As compared to previous work using an ancillary transmon statically coupled to both modes of a double-post cavity[33], this check is integrated with all the hardware needed for dual-rail single- and two-qubit gates, in a unit cell where oscillator–oscillator interactions are solely mediated via high on–off ratio coupler between individual pairs of modes. Since the coupling element mediating this beamsplitter can null any residual $ZZ$ interaction between cavities[40], we can minimize crosstalk and enable higher-fidelity two-qubit gates. Meanwhile, as compared to a joint-parity check, which asks whether the joint photon number is even, this check, which asks whether the joint photon number is zero, leverages two important features of erasure errors: that they are rare and that the state need not be preserved once an erasure is detected. Therefore, by only minimally exciting the ancilla when in the dual-rail code space, it ensures that the contribution of transmon-induced erasures and Pauli errors is subdominant at the cost of a negligible decrease in the predicted value of $p_{\mathrm{th}}$ due to the higher false negative probability. One caveat is that this check does not catch rare but damaging heating events (similarly damaging to leakage errors in conventional transmon qubit architectures). However, this could be mitigated with the addition of a joint-photon-number-selective pulse acting on the $N = 2$ manifold to form a combined erasure check and leakage reduction unit[69–74].

Improvement of the mode coherences to state-of-the-art values should enable performance substantially below the erasure threshold for the surface code. With high-fidelity state preparation, logical erasure-detected measurements, single-qubit gates and hardware-efficient mid-circuit erasure checks demonstrated, key next steps will include a fully error-detectable two-qubit gate, as well as fast qubit reset to turn leakage detection into erasure conversion.

## Methods

### Device

The device used for this experiment was previously used in Chapman et al.[40] and includes two superconducting $\lambda/4$ post cavities machined from 99.999%-purity Aluminum as the two oscillators. Into each of these cavities, we insert an EFG sapphire chip supporting a transmon qubit, a readout resonator, and a Purcell filter. These are used to prepare and readout states in the two oscillators. The transmon coupled to Bob's cavity is used to determine the spectrum in Fig. 1 and to perform the erasure check in Fig. 3. Detailed characterization of system parameters is shown in Supplementary Table II and discussed in Appendix N.

To provide the beamsplitter interaction between these cavities, we add a capacitively shunted superconducting nonlinear asymmetric inductive element (SNAIL)[56], a superconducting loop with three nominally identical Josephson junctions (each with Josephson energy $E_J/h = 90.0 \pm 0.3$ GHz) in series on one arm of the loop and a single junction (with Josephson energy $\alpha = 0.147 \pm 0.001$ times smaller) on the other. The capacitive shunt is implemented by adding leads to the two ends of the SNAIL connecting to large capacitor pads. This gives the SNAIL a charging energy $E_C/h = 177 \pm 2$ MHz, while the leads also contribute a series linear inductance with energy $E_L/h = 64 \pm 2$ GHz. This circuit is patterned onto a sapphire chip which is inserted into a tunnel that intersects both cavities, thereby generating a linear coupling between the SNAIL mode and each of the oscillator modes. Passing a DC magnetic flux through the SNAIL loop (delivered via a superconducting flux transformer) modifies the potential of the SNAIL, allowing us to generate a third-order nonlinearity. By applying a single microwave drive that couples to the charge operator of the SNAIL mode, at a frequency equal to the difference between the two cavity frequencies, we can generate the beamsplitter interaction via a three-wave-mixing process. The frequency detuning from this resonance condition is the detuning $\Delta$ indicated in Eq. (1), and the amplitude and phase of the drive determine $g_{\mathrm{bs}}$ and $\varphi$.

Any magnetic flux bias $\Phi_{\mathrm{ext}}$ besides a half-integer multiple of $\Phi_0$ gives the SNAIL a third-order nonlinearity, and at low drive powers, the magnitude of this nonlinearity determines the ratio between the applied drive amplitude and $g_{\mathrm{bs}}$. However, as was seen previously[40], at larger drive powers, this linear relationship breaks down, and there exists a maximum value of $g_{\mathrm{bs}}$ at each $\Phi_{\mathrm{ext}}$. The flux bias used in this experiment ($\Phi_{\mathrm{ext}} = 0.334\Phi_0$) was chosen to give the highest maximum value of $g_{\mathrm{bs}}$ while avoiding any unwanted resonances at any value of $g_{\mathrm{bs}}$ as it is increased to this maximum value. This, therefore, provides access to the widest range of values for $|g_{\mathrm{bs}}/\chi|$. Appendix C provides details on how we measure and calibrate the value of $g_{\mathrm{bs}}$.

The aluminum package is mounted to the mixing chamber plate of a Bluefors XLD400sl dilution refrigerator, at a temperature of 8 mK.

## Data availability

The data that support the findings of this study are available from the corresponding author upon reasonable request.

## Code availability

The code used to perform simulations is available from the corresponding author upon reasonable request.

Received: 20 June 2024; Accepted: 9 December 2024;
Published online: 07 January 2025

## References


1. Ofek, N. et al. Extending the lifetime of a quantum bit with error correction in superconducting circuits. *Nature* **536**, 441–445 (2016).
2. Flühmann, C. et al. Encoding a qubit in a trapped-ion mechanical oscillator. *Nature* **566**, 513–517 (2019).
3. Hu, L. et al. Quantum error correction and universal gate set operation on a binomial bosonic logical qubit. *Nat. Phys.* **15**, 503–508 (2019).
4. Campagne-Ibarcq, P. et al. Quantum error correction of a qubit encoded in grid states of an oscillator. *Nature* **584**, 368–372 (2020).
5. Gertler, J. M. et al. Protecting a bosonic qubit with autonomous quantum error correction. *Nature* **590**, 243–248 (2021).
6. Ni, Z. et al. Beating the break-even point with a discrete-variable-encoded logical qubit. *Nature* **616**, 56–60 (2023).
7. Sivak, V. V. et al. Real-time quantum error correction beyond break-even. *Nature* **616**, 50–55 (2023).
8. Braumüller, J. et al. Analog quantum simulation of the Rabi model in the ultra-strong coupling regime. *Nat. Commun.* **8**, 779 (2017).
9. Hu, L. et al. Simulation of molecular spectroscopy with circuit quantum electrodynamics. *Sci. Bull.* **63**, 293–299 (2018).
10. Owens, C. et al. Quarter-flux Hofstadter lattice in a qubit-compatible microwave cavity array. *Phys. Rev. A* **97**, 013818 (2018).
11. Wang, C. S. et al. Efficient multiphoton sampling of molecular vibronic spectra on a superconducting bosonic processor. *Phys. Rev. X* **10**, 021060 (2020).
12. Wang, C. S. et al. Observation of wave-packet branching through an engineered conical intersection. *Phys. Rev. X* **13**, 011008 (2023).
13. McCormick, K. C. et al. Quantum-enhanced sensing of a single-ion mechanical oscillator. *Nature* **572**, 86–90 (2019).
14. Wang, W. et al. Heisenberg-limited single-mode quantum metrology in a superconducting circuit. *Nat. Commun.* **10**, 4382 (2019).
15. Dixit, A. V. et al. Searching for dark matter with a superconducting qubit. *Phys. Rev. Lett.* **126**, 141302 (2021).
16. Wallraff, A. et al. Strong coupling of a single photon to a superconducting qubit using circuit quantum electrodynamics. *Nature* **431**, 162–167 (2004).
17. Blais, A., Huang, R. S., Wallraff, A., Girvin, S. M. & Schoelkopf, R. J. Cavity quantum electrodynamics for superconducting electrical circuits: an architecture for quantum computation. *Phys. Rev. A* **69**, 1–14 (2004).
18. Heeres, R. W. et al. Cavity state manipulation using photon-number selective phase gates. *Phys. Rev. Lett.* **115**, 137002 (2015).
19. Heeres, R. W. et al. Implementing a universal gate set on a logical qubit encoded in an oscillator. *Nat. Commun.* **8**, 94 (2017).
20. Eickbusch, A. et al. Fast universal control of an oscillator with weak dispersive coupling to a qubit. *Nat. Phys.* **18**, 1464–1469 (2022).
21. Diringer, A. A., Blumenthal, E., Grinberg, A., Jiang, L. & Hacohen-Gourgy, S. Conditional-not displacement: fast multioscillator control with a single qubit. *Phys. Rev. X* **14**, 011055 (2024).
22. Reinhold, P. et al. Error-corrected gates on an encoded qubit. *Nat. Phys.* **16**, 822–826 (2020).
23. Rosenblum, S. et al. Fault-tolerant detection of a quantum error. *Science* **361**, 266–270 (2018).
24. Sun, L. et al. Tracking photon jumps with repeated quantum non-demolition parity measurements. *Nature* **511**, 444–448 (2014).
25. Roy, S. et al. Synthetic high angular momentum spin dynamics in a microwave oscillator. arXiv:2405.15695 [quant-ph] (2024).
26. Schuster, D. I. et al. Resolving photon number states in a superconducting circuit. *Nature* **445**, 515–518 (2007).
27. Wang, H. et al. Deterministic entanglement of photons in two superconducting microwave resonators. *Phys. Rev. Lett.* **106**, 060401 (2011).
28. Gao, Y. Y. et al. Entanglement of bosonic modes through an engineered exchange interaction. *Nature* **566**, 509–512 (2019).
29. Chakram, S. et al. Multimode photon blockade. *Nat. Phys.* **18**, 879–884 (2022).
30. Wang, C. et al. A schrödinger cat living in two boxes. *Science* **352**, 1087–1091 (2016).
31. Wollack, E. A. et al. Quantum state preparation and tomography of entangled mechanical resonators. *Nature* **604**, 463–467 (2022).
32. Gertler, J. M., van Geldern, S., Shirol, S., Jiang, L. & Wang, C. Experimental realization and characterization of stabilized pair-coherent states. *PRX Quantum* **4**, 020319 (2023).
33. Koottandavida, A. et al. Erasure detection of a dual-rail qubit encoded in a double-post superconducting cavity. *Phys. Rev. Lett.* **132**, 180601 (2024).
34. Rosenblum, S. et al. A CNOT gate between multiphoton qubits encoded in two cavities. *Nat. Commun.* **9**, 652 (2018).
35. Xu, Y. et al. Demonstration of controlled-phase gates between two error-correctable photonic qubits. *Phys. Rev. Lett.* **124**, 120501 (2020).
36. Albert, V. V. et al. Pair-cat codes: autonomous error-correction with low-order nonlinearity. *Quantum Sci. Technol.* **4**, 035007 (2019).
37. Chuang, I. L., Leung, D. W. & Yamamoto, Y. Bosonic quantum codes for amplitude damping. *Phys. Rev. A* **56**, 1114–1125 (1997).
38. Chuang, I. L. & Yamamoto, Y. Simple quantum computer. *Phys. Rev. A* **52**, 3489–3496 (1995).
39. Gao, Y. Y. et al. Programmable interference between two microwave quantum memories. *Phys. Rev. X* **8**, 021073 (2018).
40. Chapman, B. J. et al. High-on–off-ratio beam-splitter interaction for gates on bosonically encoded qubits. *PRX Quantum* **4**, 020355 (2023).
41. Lu, Y. et al. High-fidelity parametric beamsplitting with a parity-protected converter. *Nat. Commun.* **14**, 5767 (2023).
42. Tsunoda, T. et al. Error-detectable bosonic entangling gates with a noisy ancilla. *PRX Quantum* **4**, 020354 (2023).
43. Teoh, J. D. et al. Dual-rail encoding with superconducting cavities. *Proc. Natl Acad. Sci. USA* **120**, e2221736120 (2023).
44. Levine, H. et al. Demonstrating a long-coherence dual-rail erasure qubit using tunable transmons. *Phys. Rev. X* **14**, 011051 (2024).
45. Grassl, M., Beth, T. & Pellizzari, T. Codes for the quantum erasure channel. *Phys. Rev. A* **56**, 33–38 (1997).
46. Kubica, A. et al. Erasure qubits: overcoming the ${T}_{1}$ limit in superconducting circuits. *Phys. Rev. X* **13**, 041022 (2023).
47. Scholl, P. et al. Erasure conversion in a high-fidelity Rydberg quantum simulator. *Nature* **622**, 273–278 (2023).
48. Wu, Y., Kolkowitz, S., Puri, S. & Thompson, J. D. Erasure conversion for fault-tolerant quantum computing in alkaline earth Rydberg atom arrays. *Nat. Commun.* **13**, 4657 (2022).
49. Kang, M., Campbell, W. C. & Brown, K. R. Quantum error correction with metastable states of trapped ions using erasure conversion. *PRX Quantum* **4**, 020358 (2023).
50. Ma, S. et al. High-fidelity gates and mid-circuit erasure conversion in an atomic qubit. *Nature* **622**, 279–284 (2023).
51. Chou, K. S. et al. A superconducting dual-rail cavity qubit with erasure-detected logical measurements. *Nat. Phys.* **20**, 1454–1460 (2024).
52. Barrett, S. D. & Stace, T. M. Fault tolerant quantum computation with very high threshold for loss errors. *Phys. Rev. Lett.* **105**, 200502 (2010).
53. Delfosse, N. & Zémor, G. Linear-time maximum likelihood decoding of surface codes over the quantum erasure channel. *Phys. Rev. Res.* **2**, 033042 (2020).
54. Reagor, M. et al. Quantum memory with millisecond coherence in circuit QED. *Phys. Rev. B* **94**, 014506 (2016).
55. Frattini, N. E. et al. 3-wave mixing Josephson dipole element. *Appl. Phys. Lett.* **110**, 222603 (2017).
56. Frattini, N. E.*Three-wave Mixing in Superconducting Circuits: Stabilizing Cats with SNAILs*. Ph.D. thesis, Yale University (2021).
57. Zhou, C. et al. Realizing all-to-all couplings among detachable quantum modules using a microwave quantum state router. *npj Quantum Inf.* **9**, 54 (2023).

58. Mollow, B. R. Power spectrum of light scattered by two-level systems. *Phys. Rev.* **188**, 1969–1975 (1969).
59. Baur, M. et al. Measurement of Autler–Townes and Mollow transitions in a strongly driven superconducting qubit. *Phys. Rev. Lett.* **102**, 243602 (2009).
60. Schwinger, J. *On Angular Momentum*. Technical Report NYO-3071 (Harvard University, Cambridge, MA, USA; Nuclear Development Associates, Inc., USA, 1952).
61. Kitaev, A. Fault-tolerant quantum computation by anyons. *Ann. Phys.* **303**, 2–30 (2003).
62. Dennis, E., Kitaev, A., Landahl, A. & Preskill, J. Topological quantum memory. *J. Math. Phys.* **43**, 4452–4505 (2002).
63. Fowler, A. G., Stephens, A. M. & Groszkowski, P. High-threshold universal quantum computation on the surface code. *Phys. Rev. A* **80**, 052312 (2009).
64. Zhang, Y. et al. Engineering bilinear mode coupling in circuit QED: theory and experiment. *Phys. Rev. A* **99**, 012314 (2019).
65. Ma, W.-L. et al. Path-independent quantum gates with noisy ancilla. *Phys. Rev. Lett.* **125**, 110503 (2020).
66. Place, A. P. M. et al. New material platform for superconducting transmon qubits with coherence times exceeding 0.3 milliseconds. *Nat. Commun.* **12**, 1779 (2021).
67. Ganjam, S. et al. Surpassing millisecond coherence in on chip superconducting quantum memories by optimizing materials and circuit design. *Nat. Commun.* **15**, 3687 (2024).
68. Oriani, A. E. et al. Niobium coaxial cavities with internal quality factors exceeding 1.5 billion for circuit quantum electrodynamics. arXiv:2403.00286 [quant-ph] (2024).
69. Aliferis, P. & Terhal, B. M. Fault-tolerant quantum computation for local leakage faults. *Quantum Inf. Comput.* **7**, 139–156 (2007).
70. Miao, K. C. et al. Overcoming leakage in quantum error correction. *Nat. Phys.* **19**, 1780–1786 (2023).
71. Marques, J. F. et al. All-microwave leakage reduction units for quantum error correction with superconducting transmon qubits. *Phys. Rev. Lett.* **130**, 250602 (2023).
72. Yang, X. et al. Coupler-assisted leakage reduction for scalable quantum error correction with superconducting qubits. *Phys. Rev. Lett.* **133**, 170601 (2024).
73. Lacroix, N. et al. Fast flux-activated leakage reduction for superconducting quantum circuits. arXiv:2309.07060 [quant-ph] (2023).
74. Thorbeck, T. et al. High-fidelity gates in a transmon using bath engineering for passive leakage reset. arXiv:2411.04101 [quant-ph] (2024).


## Acknowledgements

We acknowledge N. Ofek, P. Reinhold, and Y. Liu for their work building the FPGA firmware and software, V. Sivak for providing the Josephson Array Mode Parametric Amplifier (JAMPA), and V. Joshi, G. Liu, and M. Malnou for their work on the design and assembly of the lumped element SNAIL parametric amplifiers (LSPAs) used in the experiments. The LSPAs were fabricated by the NIST Quantum Sensors Group with support from the NIST program on scalable superconducting computing. We also thank B. Brock, K. Chou, A. Koottandavida, W. Kalfus, A. Maiti, N. Mehta, A. Narla, T. Shemma, and C. Zhou for useful discussions and feedback. This research was sponsored by the Army Research Office (ARO) under grant W911NF-23-1-0051, by the Air Force Office of Scientific Research (AFOSR) under grant FA9550-21-1-0209 and by the U.S. Department of Energy (DoE), Office of Science, National Quantum Information Science Research Centers, Co-design Center for Quantum Advantage (C2QA) under contract number DE-SC0012704. The views and conclusions contained in this document are those of the authors and should not be interpreted as representing the official policies, either expressed or implied, of the ARO, AFOSR, DoE, or the US Government. The US Government is authorized to reproduce and distribute reprints for Government purposes notwithstanding any copyright notation herein. Fabrication facilities use was supported by the Yale Institute for Nanoscience and Quantum Engineering (YINQE) and the Yale SEAS Cleanroom.

## Author contributions

S.J.d.G., S.H.X., and R.J.S. conceived the experiment. S.J.d.G, S.H.X., and B.J.C. set up the experiment hardware. B.J.C. fabricated the devices with help from L.F. J.T., T.T., P.W., and J.W.O.G. advised on characterizing error sources in the dual-rail encoding and the comparison of this erasure check to prior schemes. K.M.C. and S.P. ran simulations of the surface code threshold in the presence of false negatives. S.J.d.G. and S.H.X. performed the measurements, analyzed the data, and wrote the manuscript with input from all authors.

## Competing interests

L.F. and R.J.S. are founders and shareholders of Quantum Circuits Inc. (QCI).

## Additional information

**Supplementary information** The online version contains supplementary material available at https://doi.org/10.1038/s41534-024-00944-4.

**Correspondence** and requests for materials should be addressed to Robert J. Schoelkopf.